

## A Tale of Three: Magnetic Fields along the Orion Integral-Shaped Filament as Revealed by JCMT BISTRO survey

JINTAI WU,<sup>1,2</sup> KEPING QIU,<sup>1,2</sup> FRÉDÉRIC POIDEVIN,<sup>3,4</sup> PIERRE BASTIEN,<sup>5</sup> JUNHAO LIU,<sup>6</sup> TAO-CHUNG CHING,<sup>7</sup> TYLER L. BOURKE,<sup>8,9</sup> DEREK WARD-THOMPSON,<sup>10</sup> KATE PATTLE,<sup>11</sup> DOUG JOHNSTONE,<sup>12,13</sup> PATRICK M. KOCH,<sup>14</sup> DORIS ARZUMANIAN,<sup>15</sup> CHANG WON LEE,<sup>16,17</sup> LAPO FANCIULLO,<sup>18</sup> TAKASHI ONAKA,<sup>19</sup> JIHYE HWANG,<sup>16</sup> VALENTIN J. M. LE GOUELLEC,<sup>20,21</sup> ARCHANA SOAM,<sup>22</sup> MOTOHIDE TAMURA,<sup>23,19,24</sup> MEHRNOOSH TAHANI,<sup>25</sup> CHAKALI ESWARIAH,<sup>26</sup> HUA-BAI LI,<sup>27</sup> DAVID BERRY,<sup>28</sup> RAY S. FURUYA,<sup>29</sup> SIMON COUDÉ,<sup>30</sup> WOJIN KWON,<sup>31,32</sup> SHENG-JUN LIN,<sup>14</sup> JIA-WEI WANG,<sup>14</sup> TETSUO HASEGAWA,<sup>23</sup> SHIH-PING LAI,<sup>33,14</sup> DO-YOUNG BYUN,<sup>16,17</sup> ZHIWEI CHEN,<sup>34</sup> HUEI-RU VIVIEN CHEN,<sup>33,14</sup> WEN PING CHEN,<sup>35</sup> MIKE CHEN,<sup>13</sup> JUNGYEON CHO,<sup>36</sup> YOUNGWOO CHOI,<sup>37</sup> YUNHEE CHOI,<sup>16</sup> MINHO CHOI,<sup>16</sup> ANTONIO CHRYSOSTOMOU,<sup>8</sup> EUN JUNG CHUNG,<sup>16</sup> SOPHIA DAI,<sup>38</sup> JAMES DI FRANCESCO,<sup>12,13</sup> PHAM NGOC DIEP,<sup>39</sup> YASUO DOI,<sup>40</sup> HAO-YUAN DUAN,<sup>41</sup> YAN DUAN,<sup>38</sup> DAVID EDEN,<sup>42</sup> JASON FIEGE,<sup>43</sup> LAURA M. FISSEL,<sup>44</sup> ERICA FRANZMANN,<sup>43</sup> PER FRIBERG,<sup>28</sup> RACHEL FRIESE,<sup>45</sup> GARY FULLER,<sup>9</sup> TIM GLEDHILL,<sup>46</sup> SARAH GRAVES,<sup>28</sup> JANE GREAVES,<sup>47</sup> MATT GRIFFIN,<sup>47</sup> QILAO GU,<sup>48</sup> ILSEUNG HAN,<sup>16,17</sup> SAEKO HAYASHI,<sup>49</sup> THIEM HOANG,<sup>16,17</sup> MARTIN HOUDE,<sup>50</sup> TSUYOSHI INOUE,<sup>51</sup> SHU-ICHIRO INUTSUKA,<sup>52</sup> KAZUNARI IWASAKI,<sup>53</sup> IL-GYO JEONG,<sup>54,16</sup> VERA KÖNYVES,<sup>10</sup> JI-HYUN KANG,<sup>16</sup> MIJU KANG,<sup>16</sup> JANIK KAROLY,<sup>10</sup> AKIMASA KATAOKA,<sup>55</sup> KOJI KAWABATA,<sup>56,57,58</sup> SHINYOUNG KIM,<sup>16</sup> MI-RYANG KIM,<sup>59</sup> KYOUNG HEE KIM,<sup>60</sup> KEE-TAE KIM,<sup>16,17</sup> JONGSOO KIM,<sup>16,17</sup> HYOSUNG KIM,<sup>31</sup> GWANJEONG KIM,<sup>61</sup> FLORIAN KIRCHSCHLAGER,<sup>62</sup> JASON KIRK,<sup>10</sup> MASATO I.N. KOBAYASHI,<sup>63</sup> TAKAYOSHI KUSUNE,<sup>64</sup> JUNGMI KWON,<sup>19</sup> KEVIN LACAILE,<sup>65,66</sup> CHI-YAN LAW,<sup>27,67</sup> HYESEUNG LEE,<sup>68</sup> CHIN-FEI LEE,<sup>14</sup> SANG-SUNG LEE,<sup>16,17</sup> JEONG-EUN LEE,<sup>69</sup> DALEI LI,<sup>70</sup> DI LI,<sup>71,72</sup> GUANGXING LI,<sup>73</sup> SHENG-YUAN LIU,<sup>14</sup> TIE LIU,<sup>74</sup> HONG-LI LIU,<sup>75</sup> XING LU,<sup>48</sup> A-RAN LYO,<sup>16</sup> STEVE MAIRS,<sup>28</sup> MASAFUMI MATSUMURA,<sup>76</sup> BRENDA MATTHEWS,<sup>12,13</sup> GERALD MORIARTY-SCHIEVEN,<sup>12</sup> TETSUYA NAGATA,<sup>77</sup> FUMITAKA NAKAMURA,<sup>55,78</sup> HIROYUKI NAKANISHI,<sup>79</sup> NGUYEN BICH NGOC,<sup>39,80</sup> NAGAYOSHI OHASHI,<sup>14</sup> GEUMSOOK PARK,<sup>16</sup> HARRIET PARSONS,<sup>28</sup> NICOLAS PERETTO,<sup>47</sup> FELIX PRIESTLEY,<sup>47</sup> TAE-SOO PYO,<sup>78,81</sup> LEI QIAN,<sup>71</sup> RAMPRASAD RAO,<sup>14</sup> JONATHAN RAWLINGS,<sup>11</sup> MARK RAWLINGS,<sup>28</sup> BRENDAN RETTER,<sup>47</sup> JOHN RICHER,<sup>82,83</sup> ANDREW RIGBY,<sup>47</sup> SARAH SADAVOY,<sup>44</sup> HIRO SAITO,<sup>84</sup> GIORGIO SAVINI,<sup>85</sup> MASUMICHI SETA,<sup>86</sup> EKTA SHARMA,<sup>71</sup> YOSHITO SHIMAJIRI,<sup>87</sup> HIROKO SHINNAGA,<sup>79</sup> YA-WEN TANG,<sup>14</sup> XINDI TANG,<sup>88</sup> HOANG DUC THUONG,<sup>89</sup> KOHJI TOMISAKA,<sup>55</sup> LE NGOC TRAM,<sup>90</sup> YUSUKE TSUKAMOTO,<sup>79</sup> SERENA VITI,<sup>91</sup> HONGCHI WANG,<sup>34</sup> ANTHONY WHITWORTH,<sup>47</sup> JINJIN XIE,<sup>38</sup> MENG-ZHE YANG,<sup>33</sup> HSI-WEI YEN,<sup>14</sup> HYUNJU YOO,<sup>36</sup> JINGHUA YUAN,<sup>38</sup> HYEONG-SIK YUN,<sup>16</sup> TETSUYA ZENKO,<sup>77</sup> GUOYIN ZHANG,<sup>71</sup> CHUAN-PENG ZHANG,<sup>38,71</sup> YAPENG ZHANG,<sup>92</sup> JIANJUN ZHOU,<sup>70</sup> LEI ZHU,<sup>71</sup> ILSE DE LOOZE,<sup>62</sup> PHILIPPE ANDRÉ,<sup>93</sup> C. DARREN DOWELL,<sup>94</sup> STEWART EYRES,<sup>95</sup> SAM FALLE,<sup>96</sup> JEAN-FRANÇOIS ROBITAILLE,<sup>97</sup> AND SVEN VAN LOO<sup>98</sup>

<sup>1</sup>School of Astronomy and Space Science, Nanjing University, 163 Xianlin Avenue, Nanjing 210023, People's Republic of China

<sup>2</sup>Key Laboratory of Modern Astronomy and Astrophysics (Nanjing University), Ministry of Education, Nanjing 210023, People's Republic of China

<sup>3</sup>Instituto de Astrofísica de Canarias, E-38205 La Laguna, Tenerife, Canary Islands, Spain

<sup>4</sup>Universidad de La Laguna, Dpto. Astrofísica, E-38206 La Laguna, Tenerife, Spain

<sup>5</sup>Centre de recherche en astrophysique du Québec & département de physique, Université de Montréal, 1375, Avenue Thérèse-Lavoie-Roux, Montréal, QC, H2V 0B3, Canada

<sup>6</sup>Division of ALMA, National Astronomical Observatory of Japan, Mitaka, Tokyo 181-8588, Japan

<sup>7</sup>Zhejiang Lab, Kechuang Avenue, Yuhang District, Hangzhou 311121, People's Republic of China

<sup>8</sup>SKA Observatory, Jodrell Bank, Lower Withington, Macclesfield SK11 9FT, UK

<sup>9</sup>Jodrell Bank Centre for Astrophysics, School of Physics and Astronomy, University of Manchester, Oxford Road, Manchester, M13 9PL, UK

<sup>10</sup>Jeremiah Horrocks Institute, University of Central Lancashire, Preston PR1 2HE, UK

<sup>11</sup>Department of Physics and Astronomy, University College London, WC1E 6BT London, UK

<sup>12</sup>NRC Herzberg Astronomy and Astrophysics, 5071 West Saanich Road, Victoria, BC V9E 2E7, Canada

<sup>13</sup>Department of Physics and Astronomy, University of Victoria, Victoria, BC V8W 2Y2, Canada

<sup>14</sup>Academia Sinica Institute of Astronomy and Astrophysics, No.1, Sec. 4., Roosevelt Road, Taipei 10617, Taiwan

<sup>15</sup>Division of Science, National Astronomical Observatory of Japan, 2-21-1 Osawa, Mitaka, Tokyo 181-8588, Japan

<sup>16</sup>Korea Astronomy and Space Science Institute, 776 Daedeokdae-ro, Yuseong-gu, Daejeon 34055, Republic of Korea

<sup>17</sup>University of Science and Technology, Korea, 217 Gajeong-ro, Yuseong-gu, Daejeon 34113, Republic of Korea

- <sup>18</sup>National Chung Hsing University, 145 Xingda Rd., South Dist., Taichung City 402, Taiwan
- <sup>19</sup>Department of Astronomy, Graduate School of Science, The University of Tokyo, 7-3-1 Hongo, Bunkyo-ku, Tokyo 113-0033, Japan
- <sup>20</sup>NASA Ames Research Center, Space Science and Astrobiology Division M.S. 245-6 Moffett Field, CA 94035, USA
- <sup>21</sup>NASA Postdoctoral Program Fellow
- <sup>22</sup>Indian Institute of Astrophysics, II Block, Koramangala, Bengaluru 560034, India
- <sup>23</sup>National Astronomical Observatory of Japan, National Institutes of Natural Sciences, Osawa, Mitaka, Tokyo 181-8588, Japan
- <sup>24</sup>Astrobiology Center, National Institutes of Natural Sciences, 2-21-1 Osawa, Mitaka, Tokyo 181-8588, Japan
- <sup>25</sup>Banting and KIPAC Fellow: Kavli Institute for Particle Astrophysics and Cosmology (KIPAC), Stanford University, Stanford, CA, United States
- <sup>26</sup>Indian Institute of Science Education and Research (IISER) Tirupati, Rami Reddy Nagar, Karakambadi Road, Mangalam (P.O.), Tirupati 517 507, India
- <sup>27</sup>Department of Physics, The Chinese University of Hong Kong, Shatin, N.T., Hong Kong
- <sup>28</sup>East Asian Observatory, 660 N. A'ohōkū Place, University Park, Hilo, HI 96720, USA
- <sup>29</sup>Institute of Liberal Arts and Sciences Tokushima University, Minami Jousanajima-machi 1-1, Tokushima 770-8502, Japan
- <sup>30</sup>SOFIA Science Center, Universities Space Research Association, NASA Ames Research Center, Moffett Field, California 94035, USA
- <sup>31</sup>Department of Earth Science Education, Seoul National University, 1 Gwanak-ro, Gwanak-gu, Seoul 08826, Republic of Korea
- <sup>32</sup>SNU Astronomy Research Center, Seoul National University, 1 Gwanak-ro, Gwanak-gu, Seoul 08826, Republic of Korea
- <sup>33</sup>Institute of Astronomy and Department of Physics, National Tsing Hua University, Hsinchu 30013, Taiwan
- <sup>34</sup>Purple Mountain Observatory, Chinese Academy of Sciences, 2 West Beijing Road, 210008 Nanjing, People's Republic of China
- <sup>35</sup>Institute of Astronomy, National Central University, Zhongli 32001, Taiwan
- <sup>36</sup>Department of Astronomy and Space Science, Chungnam National University, 99 Daehak-ro, Yuseong-gu, Daejeon 34134, Republic of Korea
- <sup>37</sup>Department of Physics and Astronomy, Seoul National University, 1 Gwanak-ro, Gwanak-gu, Seoul 08826, Republic of Korea
- <sup>38</sup>National Astronomical Observatories, Chinese Academy of Sciences, A20 Datun Road, Chaoyang District, Beijing 100012, People's Republic of China
- <sup>39</sup>Vietnam National Space Center, Vietnam Academy of Science and Technology, 18 Hoang Quoc Viet, Hanoi, Vietnam
- <sup>40</sup>Department of Earth Science and Astronomy, Graduate School of Arts and Sciences, The University of Tokyo, 3-8-1 Komaba, Meguro, Tokyo 153-8902, Japan
- <sup>41</sup>Taipei Astronomical Museum 111013 No.363, Jihe Rd., Shilin Dist., Taipei, Taiwan, R.O.C
- <sup>42</sup>Armagh Observatory and Planetarium, College Hill, Armagh BT61 9DG, UK
- <sup>43</sup>Department of Physics and Astronomy, The University of Manitoba, Winnipeg, Manitoba R3T2N2, Canada
- <sup>44</sup>Department for Physics, Engineering Physics and Astrophysics, Queen's University, Kingston, ON, K7L 3N6, Canada
- <sup>45</sup>National Radio Astronomy Observatory, 520 Edgemont Road, Charlottesville, VA 22903, USA
- <sup>46</sup>School of Physics, Astronomy & Mathematics, University of Hertfordshire, College Lane, Hatfield, Hertfordshire AL10 9AB, UK
- <sup>47</sup>School of Physics and Astronomy, Cardiff University, The Parade, Cardiff, CF24 3AA, UK
- <sup>48</sup>Shanghai Astronomical Observatory, Chinese Academy of Sciences, 80 Nandan Road, Shanghai 200030, People's Republic of China
- <sup>49</sup>Kavli Institute for the Physics and Mathematics of the Universe, The University of Tokyo, 5-1-5 Kashiwanoha, Kashiwa, Chiba, 277-8583, Japan
- <sup>50</sup>Department of Physics and Astronomy, The University of Western Ontario, 1151 Richmond Street, London N6A 3K7, Canada
- <sup>51</sup>Department of Physics, Konan University, Okamoto 8-9-1, Higashinada-ku, Kobe 658-8501, Japan
- <sup>52</sup>Department of Physics, Graduate School of Science, Nagoya University, Furo-cho, Chikusa-ku, Nagoya 464-8602, Japan
- <sup>53</sup>Center for Computational Astrophysics, National Astronomical Observatory of Japan, Mitaka, Tokyo 181-8588, Japan
- <sup>54</sup>Department of Astronomy and Atmospheric Sciences, Kyungpook National University, Daegu 41566, Republic of Korea
- <sup>55</sup>Division of Theoretical Astronomy, National Astronomical Observatory of Japan, Mitaka, Tokyo 181-8588, Japan
- <sup>56</sup>Hiroshima Astrophysical Science Center, Hiroshima University, Kagamiyama 1-3-1, Higashi-Hiroshima, Hiroshima 739-8526, Japan
- <sup>57</sup>Department of Physics, Hiroshima University, Kagamiyama 1-3-1, Higashi-Hiroshima, Hiroshima 739-8526, Japan
- <sup>58</sup>Core Research for Energetic Universe (CORE-U), Hiroshima University, Kagamiyama 1-3-1, Higashi-Hiroshima, Hiroshima 739-8526, Japan
- <sup>59</sup>School of Space Research, Kyung Hee University, 1732 Deogyong-daero, Giheung-gu, Yongin-si, Gyeonggi-do 17104, Republic of Korea
- <sup>60</sup>Ulsan National Institute of Science and Technology (UNIST), UNIST-gil 50, Eonyang-eup, Ulju-gun, Ulsan 44919, Republic of Korea
- <sup>61</sup>Nobeyama Radio Observatory, National Astronomical Observatory of Japan, National Institutes of Natural Sciences, Nobeyama, Minamimaki, Minamisaku, Nagano 384-1305, Japan
- <sup>62</sup>Sterrenkundig Observatorium, Ghent University, Krijgslaan 281-S9, 9000 Gent, BE
- <sup>63</sup>Physikalisches Institut, University of Cologne, Zùlpicher Str. 77, D-50937 Köln, Germany
- <sup>64</sup>Astronomical Institute, Graduate School of Science, Tohoku University, Aoba-ku, Sendai, Miyagi 980-8578, Japan
- <sup>65</sup>Department of Physics and Astronomy, McMaster University, Hamilton, ON L8S 4M1 Canada
- <sup>66</sup>Department of Physics and Atmospheric Science, Dalhousie University, Halifax B3H 4R2, Canada
- <sup>67</sup>Department of Space, Earth & Environment, Chalmers University of Technology, SE-412 96 Gothenburg, Sweden

- <sup>68</sup> *Ulsan National Institute of Science and Technology (UNIST), 50 UNIST-gil, Ulsan 44919, Republic of Korea*
- <sup>69</sup> *Astronomy Program, Department of Physics and Astronomy, Seoul National University, 1 Gwanak-ro, Gwanak-gu, Seoul 08826, Republic of Korea*
- <sup>70</sup> *Xinjiang Astronomical Observatory, Chinese Academy of Sciences, 150 Science 1-Street, Urumqi 830011, Xinjiang, People's Republic of China*
- <sup>71</sup> *CAS Key Laboratory of FAST, National Astronomical Observatories, Chinese Academy of Sciences, People's Republic of China*  
<sup>72</sup> *University of Chinese Academy of Sciences, Beijing 100049, People's Republic of China*
- <sup>73</sup> *South-Western Institute for Astronomy Research, Yunnan University, Kunming 650500, People's Republic of China*
- <sup>74</sup> *Key Laboratory for Research in Galaxies and Cosmology, Shanghai Astronomical Observatory, Chinese Academy of Sciences, 80 Nandan Road, Shanghai 200030, People's Republic of China*  
<sup>75</sup> *Department of Astronomy, Yunnan University, Kunming, 650091, PR China*
- <sup>76</sup> *Faculty of Education & Center for Educational Development and Support, Kagawa University, Saiwai-cho 1-1, Takamatsu, Kagawa, 760-8522, Japan*  
<sup>77</sup> *Department of Astronomy, Graduate School of Science, Kyoto University, Sakyo-ku, Kyoto 606-8502, Japan*  
<sup>78</sup> *SOKENDAI (The Graduate University for Advanced Studies), Hayama, Kanagawa 240-0193, Japan*
- <sup>79</sup> *Department of Physics and Astronomy, Graduate School of Science and Engineering, Kagoshima University, 1-21-35 Korimoto, Kagoshima, Kagoshima 890-0065, Japan*
- <sup>80</sup> *Graduate University of Science and Technology, Vietnam Academy of Science and Technology, 18 Hoang Quoc Viet, Cau Giay, Hanoi, Vietnam*  
<sup>81</sup> *Subaru Telescope, National Astronomical Observatory of Japan, 650 N. A'ohōkū Place, Hilo, HI 96720, USA*  
<sup>82</sup> *Astrophysics Group, Cavendish Laboratory, J. J. Thomson Avenue, Cambridge CB3 0HE, UK*
- <sup>83</sup> *Kavli Institute for Cosmology, Institute of Astronomy, University of Cambridge, Madingley Road, Cambridge, CB3 0HA, UK*
- <sup>84</sup> *Faculty of Pure and Applied Sciences, University of Tsukuba, 1-1-1 Tennodai, Tsukuba, Ibaraki 305-8577, Japan*  
<sup>85</sup> *OSL, Physics & Astronomy Dept., University College London, WC1E 6BT London, UK*
- <sup>86</sup> *Department of Physics, School of Science and Technology, Kwansei Gakuin University, 2-1 Gakuen, Sanda, Hyogo 669-1337, Japan*  
<sup>87</sup> *Kyushu Kyoritsu University, 1-8, Jiyugaoka, Yahatanishi-ku, Kitakyushu-shi, Fukuoka 807-8585, Japan*
- <sup>88</sup> *Xinjiang Astronomical Observatory, Chinese Academy of Sciences, 830011 Urumqi, People's Republic of China*  
<sup>89</sup> *School of Physics and Astronomy, University of Minnesota, Minneapolis, MN 55455, USA*
- <sup>90</sup> *University of Science and Technology of Hanoi, Vietnam Academy of Science and Technology, 18 Hoang Quoc Viet, Hanoi, Vietnam*  
<sup>91</sup> *Physics & Astronomy Dept., University College London, WC1E 6BT London, UK*  
<sup>92</sup> *Department of Astronomy, Beijing Normal University, Beijing 100875, China*
- <sup>93</sup> *Laboratoire AIM CEA/DSM-CNRS-Université Paris Diderot, IRFU/Service d'Astrophysique, CEA Saclay, F-91191 Gif-sur-Yvette, France*  
<sup>94</sup> *Jet Propulsion Laboratory, M/S 169-506, 4800 Oak Grove Drive, Pasadena, CA 91109, USA*  
<sup>95</sup> *University of South Wales, Pontypridd, CF37 1DL, UK*
- <sup>96</sup> *Department of Applied Mathematics, University of Leeds, Woodhouse Lane, Leeds LS2 9JT, UK*  
<sup>97</sup> *Univ. Grenoble Alpes, CNRS, IPAG, 38000 Grenoble, France*
- <sup>98</sup> *School of Physics and Astronomy, University of Leeds, Woodhouse Lane, Leeds LS2 9JT, UK*

## ABSTRACT

As part of the BISTRO survey, we present JCMT 850  $\mu\text{m}$  polarimetric observations towards the Orion Integral-Shaped Filament (ISF) that covers three portions known as OMC-1, OMC-2, and OMC-3. The magnetic field threading the ISF seen in the JCMT POL-2 map appears as a tale of three: pinched for OMC-1, twisted for OMC-2, and nearly uniform for OMC-3. A multi-scale analysis shows that the magnetic field structure in OMC-3 is very consistent at all the scales, whereas the field structure in OMC-2 shows no correlation across different scales. In OMC-1, the field retains its mean orientation from large to small scales, but shows some deviations at small scales. Histograms of relative orientations between the magnetic field and filaments reveal a bimodal distribution for OMC-1, a relatively random distribution for OMC-2, and a distribution with a predominant peak at  $90^\circ$  for OMC-3. Furthermore, the magnetic fields in OMC-1 and OMC-3 both appear to be aligned perpendicular to the fibers, which are denser structures within the filament, but the field in OMC-2 is aligned along with the fibers. All these suggest that gravity, turbulence, and magnetic field are each playing a leading role in OMC-1, 2, and 3, respectively. While OMC-2 and 3 have almost the same gas mass, density, and non-thermal velocity dispersion, there are on average younger and fewer young stellar objects in OMC-3, providing evidence that a stronger magnetic field will induce slower and less efficient star formation in molecular clouds.

*Keywords:* Star formation(1569); Interstellar magnetic fields(845); Interstellar clouds(834); Polarimetry(1278)

## 1. INTRODUCTION

During the star formation process, the dynamics and physical states of the molecular clouds are influenced by various physical mechanisms, especially self-gravity, turbulence and magnetic field ( $B$ -field) (McKee & Ostriker 2007). It has long been a subject of intense debate as to which force is playing a dominant role in regulating the cloud collapse and fragmentation (Mac Low & Klessen 2004; Mouschovias et al. 2006; Crutcher 2012). Regarding the  $B$ -field, either the “strong-field models” which support a defining role played by the  $B$ -field (e.g., Mouschovias et al. 2006), or the “weak-field models” that pay more attention to turbulence (e.g., Mac Low & Klessen 2004), cannot sufficiently explain all the observations towards star formation regions. The relative importance of turbulence and  $B$ -field as well as their interactions with self-gravity in star formation remain to be explored in more case studies (Li 2021). More reasonable scenarios may need to consider essential roles of both processes, which have been explored in simulations (Crutcher 2012; Hennebelle & Inutsuka 2019).

Dense molecular filaments are important sites for star formation, with molecular gas accumulating and then fragmenting into star-forming cores due to gravitational instability (André et al. 2014; Pineda et al. 2023; Hacar et al. 2023). Observations have shown that  $B$ -fields appear to be perpendicular to high-density filaments, while they appear to be parallel to low-density elongated clouds or striations (e.g., Cox et al. 2016). Magnetic fields may also play a central role in shaping the fragmentation and physical states of filaments (e.g., Tang et al. 2019; Arzoumanian et al. 2021). More observations and dedicated studies are needed to revealing the relative importance of  $B$ -field compared to other processes and to decipher how  $B$ -field influence the gas dynamics during filament formation and fragmentation.

Situated on the head of the Orion A giant molecular cloud, the Integral-Shaped Filament (ISF) is a well-known nearby star-forming filament (Johnstone & Bally 1999; Bally 2008) containing several portions, of which the more extensively studied are OMC-1, OMC-2, and OMC-3. Several studies present  $B$ -field results of the whole ISF (e.g., Houde et al. 2004; Matthews et al. 2009), or its portions OMC-1 (e.g., Ward-Thompson et al. 2017; Chuss et al. 2019; Ajeddig et al. 2022), OMC-2/3 (Poidevin et al. 2010; Zielinski & Wolf 2022; Li et al. 2022), and OMC-4 (Li et al. 2022). With active massive star formation, the  $B$ -field in OMC-1 has been detected with a large-scale hourglass morphology associated with two molecular clumps, namely Orion BN/KL and South (e.g., Schleuning 1998; Ward-Thompson et al. 2017; Pattle et al. 2017). The  $B$ -field orientations in OMC-2 exhibit more variations compared to the other portions of the ISF (e.g., Poidevin et al. 2010). As for OMC-3, observations have revealed a more ordered  $B$ -field (e.g., Matthews et al. 2001). Therefore, being the nearest filamentary molecular cloud (393 pc, Großschedl et al. 2018) forming both massive and intermediate- to low-mass stars, the OMC-1/2/3 region shows hints of varying  $B$ -field properties along the ISF, and a more comprehensive investigation is expected to provide new insights into the role of  $B$ -fields in filament dynamics and star formation. In this current work, as part of the  $B$ -fields In Star-forming Region Observations (BISTRO, Ward-Thompson et al. 2017; Bastien 2020), we use the James Clerk Maxwell Telescope (JCMT) to make submm polarimetric observations of the ISF. The BISTRO team has previously observed the ISF (Ward-Thompson et al. 2017; Pattle et al. 2017). However, those observations were focused only on OMC-1. In this paper we have more than doubled the area studied, to also include OMC-2 and 3. The aim is to set those earlier observations in the context of their environment and to understand the bigger picture of the role of magnetic fields in Orion A.

## 2. OBSERVATIONS

The observations of polarized dust emission (project ID: M17BL011, M20AL018) covering the OMC-1, 2, and 3 in the Orion ISF were performed using POL-2 (Friberg et al. 2016) together with SCUBA-2 (Holland et al. 2013) on the JCMT. Some observations (project ID: M15BEC02) toward OMC-1 south were taken during the POL-2 commissioning stage. All the data were obtained using the POL-2 DAISY mode (Friberg et al. 2016).

The reduction of raw data involves three primary steps and uses two packages SMURF and KAPPA (Jenness et al. 2013; Currie & Berry 2014) in the Starlink package (Currie et al. 2014). With an effective beam size of  $14.1''$  ( $\sim 0.027$  pc at 393 pc) at  $850 \mu\text{m}$  (Dempsey et al. 2013), we produced a synthesized map of Stokes parameters using a pixel size of  $4''$ . We perform the absolute flux calibration with the flux conversion factor (FCF) estimated by adopting different

recommended FCF values (Mairs et al. 2021) weighted with the observation time. In our work, FCFs were set to 695 Jy beam<sup>-1</sup> pW<sup>-1</sup> for OMC-1, and to 668 Jy beam<sup>-1</sup> pW<sup>-1</sup> for OMC-2, 3.

By using three models including background, source, and residual components, we smoothed the polarization maps to revise some obviously inaccurate measurements due to the uncertainty. With the calibrated Stokes parameters, the polarized intensities ( $PI$ ), polarization degrees ( $P$ ), and angles ( $\theta_P$ ) at different positions can be calculated using the following equations:

$$PI = \sqrt{Q^2 + U^2}, \quad P = \frac{PI}{I}, \quad \text{and} \quad \theta_P = 0.5 \tan^{-1}\left(\frac{U}{Q}\right). \quad (1)$$

Since both positive and negative  $Q$  and  $U$  values contribute to a positive  $PI$  value, a modified asymptotic estimator (MAS, Plaszczyński et al. 2014) is employed to de-bias the results to avoid the overestimation of  $PI$ .

Using these equations, the parameters and their uncertainties are determined to produce a catalogue of polarization half-vectors. The polarization vectors with  $P/\sigma_P < 3$  or  $\sigma_P > 5\%$  are removed in our analysis, where  $\sigma_P$  is the uncertainty of polarization degree. All the selected polarization vectors, with their lengths proportional to the polarization degrees and plotted in an interval of  $8''$ , are all shown in Figure 1(a).

### 3. RESULTS

#### 3.1. Magnetic field morphology

Assuming aligned dust grains regulated by  $B$ -fields based on the Radiation Alignment Theory (RAT) (Lazarian 2007), the polarization angles of thermal dust emission enable one to infer the orientation of the  $B$ -field projected on the plane of sky. Figure 1(b-d) shows the statistics of  $B$ -field orientation distributions of the three clouds. It is clear that the  $B$ -fields in OMC-1 are mostly aligned along a northwest-southeast orientation with a position angle (PA) of about  $120^\circ$ , while the  $B$ -fields in OMC-3 are predominantly aligned along a northeast-southwest orientation with a PA of about  $45^\circ$ . On the other hand, the  $B$ -field orientations in OMC-2 have a broad distribution between  $50^\circ$  and  $130^\circ$  and another group between  $0^\circ$  and  $30^\circ$ , indicating a relatively more random distribution. In Figure 1(e), we present the half-vectors rotated by  $90^\circ$  in an interval of  $20''$  representing the corresponding  $B$ -field orientations across the filament.

**OMC-1:** Overall, the  $B$ -field appears to be perpendicular to the main axis of the cloud/filament. OMC-1 is associated with the Orion Nebula Cluster (ONC) and contains a high concentration of gas at a high temperature of  $>100\text{K}$  (e.g., Li et al. 2020). The maximum  $850\mu\text{m}$  brightness of OMC-1 is approximately  $9 \times 10^5$  mJy/beam, and is associated with the hot, high-mass star-forming clumps of Orion BN/KL. Moreover, as one approaches the location of Orion BN/KL, the hourglass pattern of the  $B$ -field becomes more prominent. This pinched morphology in the central cloud of OMC-1 indicates a strong interaction between gravity and  $B$ -field, showcasing the effects of the  $B$ -field in high-mass star forming regions. Figure 1 also shows  $B$ -field lines that are aligned parallel with the orientation of the cloud extension in the northeastern sub-filament of OMC-1, suggesting a gas accumulation process that is guided by the  $B$ -field surrounding the filament.

**OMC-2:** Our dust polarization map of OMC-2 is a marked improvement over previous observations, such as the SCUPOL results (Poidevin et al. 2010). As a site for intermediate-to-low mass star formation, OMC-2 seems to have relatively chaotic  $B$ -field structures compared to the other two clouds. From Figure 1(e), the  $B$ -field lines seem to converge towards denser areas in the central parts of OMC-2, where gravitational contraction is likely taking place. In contrast, a sub-filament to the west of the main filament is overall perpendicular to the  $B$ -field.

**OMC-3:** OMC-3 appears to be a filamentary cloud extending from southeast to northwest. The POL-2 observations reveal a nearly uniform  $B$ -field in the northern backbone of OMC-3. However, the OMC-3 South, which is suspected to be a "second filament" as noted by Poidevin et al. (2010), has disorderly  $B$ -field directions that are similar to the complicated structures of OMC-2. In the main body of OMC-3 North, the  $B$ -field orientations are orthogonal to the filament direction. In brief, OMC-3 exhibits very ordered to even uniform  $B$ -field structures.

#### 3.2. Multi-scale view of $B$ -field geometries in Orion ISF

We utilized the 353 GHz polarization observations made with the High Frequency Instrument (HFI) on *Planck* to infer the large-scale  $B$ -field (Planck Collaboration et al. 2015). The Stokes  $I$ ,  $Q$ , and  $U$  maps, which were corrected for the contamination from the Cosmic Microwave Background (CMB) and Cosmic Infrared Background (CIB), were used to generate the large-scale polarization map at a resolution of  $5'$ . Figure 2(a) displays the large-scale  $B$ -field maps

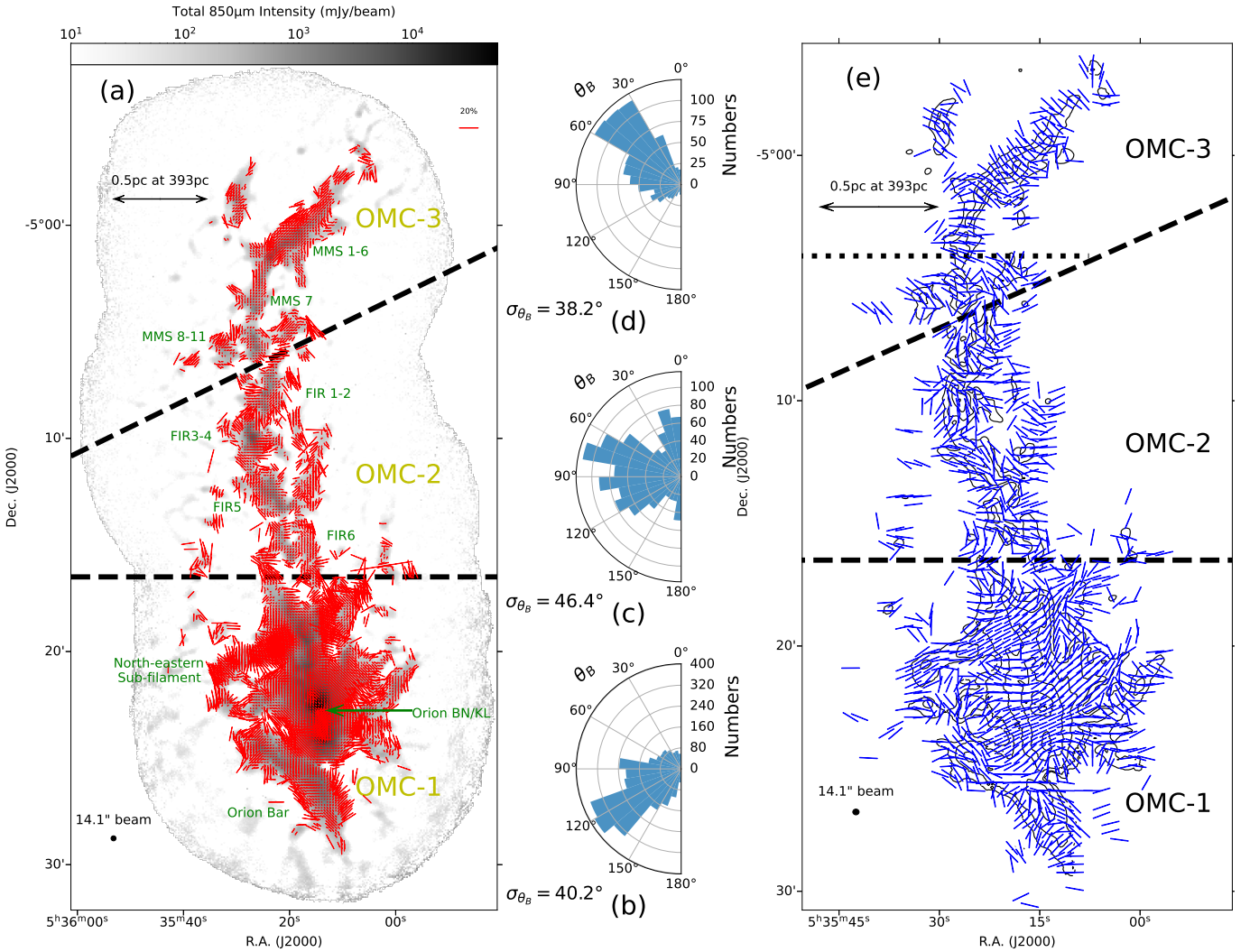


**Figure 1.** Panel (a): Dust polarization observations of Orion A ISF made with the POL-2 on JCMT. Grayscale image shows the 850  $\mu\text{m}$  total intensity (Stokes  $I$ ). Red vectors are plotted in an interval of  $8''$ , showing the polarization angles with the length proportional to the polarization degree. Black dashed lines mark the divisions between three clouds, i.e., OMC-1 to the south, OMC-2 in the middle, and OMC-3 to the north. The locations of the 1.3 mm sources identified by Chini et al. (1997) including MMS 1-10 in OMC-3, FIR 1-6 in OMC-2, and the Northeastern Sub-filament and Orion Bar in OMC-1 are marked on the image. Panels (b), (c), and (d) show the histograms of the position angles of the  $B$ -field orientations for OMC-1, OMC-2, and OMC-3, respectively. Panel (e): Blue vectors with a uniform arbitrary length are plotted in an interval of  $20''$ , showing the magnetic field orientations, and are derived by rotating the polarization vectors by  $90^\circ$ . The 850  $\mu\text{m}$  total intensity is shown in black contours at  $\log_{10}$  scale ( $\text{mJy beam}^{-1}$ ), which starts from 2.2 and continues at steps of 0.5

. The black dotted line splits the OMC-3 cloud into the North and South parts.

around the Orion A region. The  $B$ -field is roughly perpendicular to the ISF. Moreover, the field structure appears slightly pinched toward the filament.

In addition, we check the optical starlight polarization observations to further explore the large-scale  $B$ -field in relatively low-density regions (Poidevin et al. 2011). To limit our analysis to sources within the Orion cloud, we only consider starlight detections that fall within the region of our JCMT observations and have a distance of  $360\sim 500$  pc based on Gaia parallax measurements (Rezaei Kh. et al. 2020; Gaia Collaboration et al. 2021; Bailer-Jones et al. 2021). The  $B$ -fields derived from 61 detections are shown in Figure 2(b). The majority of the  $B$ -field half-vectors have a west-east or northeast-southwest orientation, in general consistent with the *Planck* results. Given the optical polarization data are presumably tracing the  $B$ -field threading the ISM around the ISF or that in the foreground toward the ISF, the  $B$ -field structure shows small deviation compared to that seen in the *Planck* map.

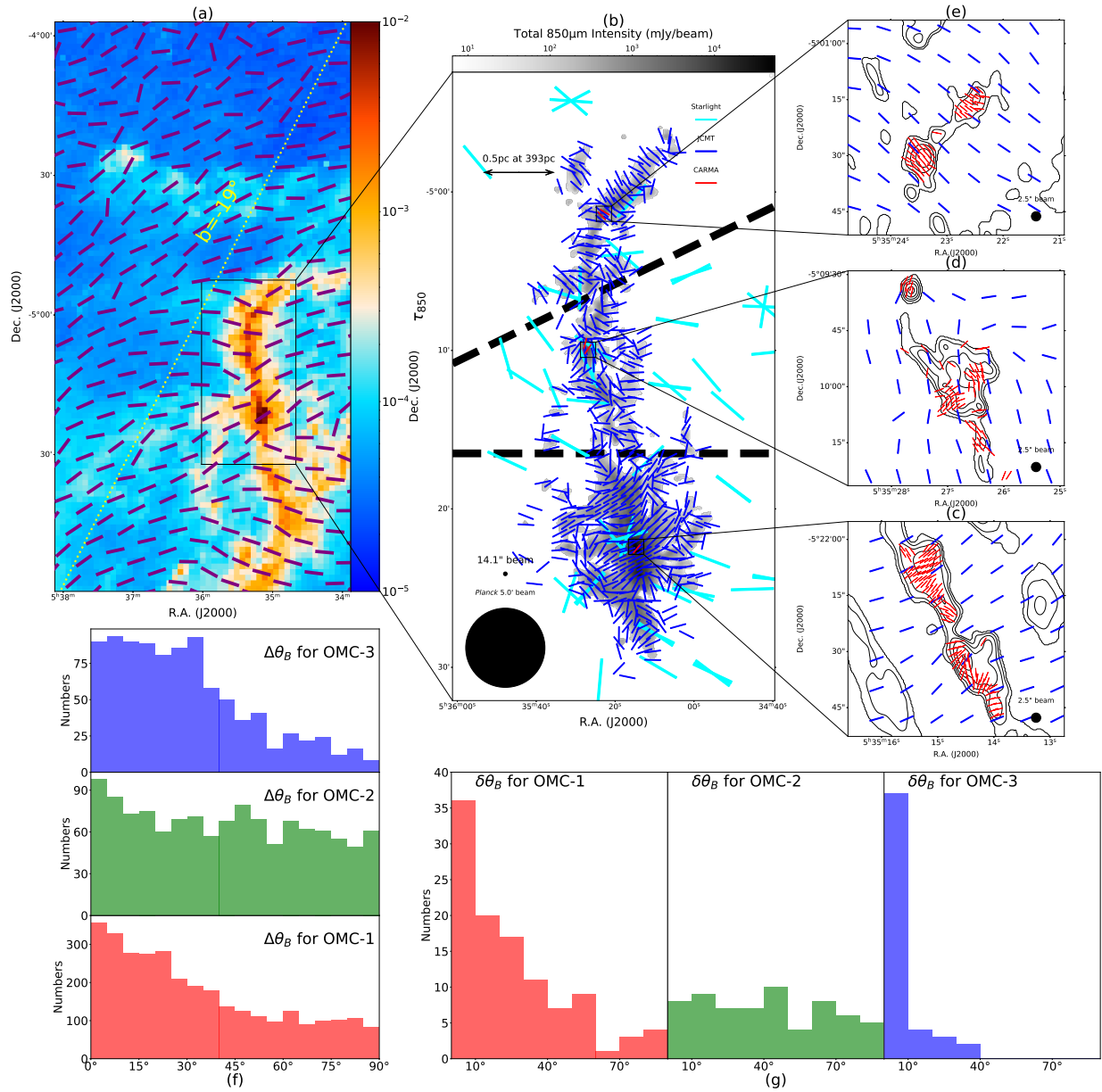


**Figure 2.** Multi-scale  $B$ -field orientations in the ISF. Panel (a): the background image displays  $850\ \mu\text{m}$  opacity map obtained from the *Herschel* and *Planck* data (Lombardi et al. 2014); purple segments indicate the large-scale  $B$ -field orientations inferred from the *Planck* 353 GHz data. A yellow dotted line marks the galactic latitude  $b=19^\circ$ . Panel (b):  $B$ -field orientations derived from starlight, JCMT POL-2, and CARMA observations. The background image shows the JCMT  $850\ \mu\text{m}$  total intensity map; blue vectors plotted at an interval of  $32''$  denote the  $B$ -field orientations observed by JCMT POL-2; cyan vectors represent the  $B$ -field orientations revealed by starlight polarization observations (Poidevin et al. 2011); red vectors show the averaged  $B$ -field orientations obtained by the CARMA TADPOL survey (Hull et al. 2014). In Panels (c), (d), and (e), red vectors indicate the  $B$ -field orientations obtained by the CARMA TADPOL survey in selected dense cores located in OMC-1, OMC-2, and OMC-3, respectively; blue vectors show the  $B$ -field orientations derived with the JCMT POL-2 observations; the CARMA observations of the total dust emission at  $1.3\ \text{mm}$  are shown in black contours at  $\log_{10}$  scale ( $\text{mJy beam}^{-1}$ ), which starts from  $-2.0$  and continues at steps of  $0.5$  in Panel (c), starts from  $-2.0$  and continues at steps of  $0.2$  in Panel (d), starts from  $-1.0$  and continues at steps of  $0.3$  in Panel (e). Panel (f): Histograms of the difference angles between the  $B$ -field orientations unveiled by *Planck* and that by the JCMT POL-2 for OMC-1, OMC-2, and OMC-3. Panel (g): Histograms of the difference angles between the  $B$ -field orientations obtained by the JCMT POL-2 and that by the CARMA TADPOL survey for OMC-1, OMC-2, and OMC-3.

The TADPOL survey (Hull et al. 2014) mapped the  $B$ -fields toward several selected sources in the ISF, including Orion KL in OMC-1, FIR 3 and FIR 4 in OMC-2, and MMS 5 and MMS 6 in OMC-3, at an angular resolution of  $2.5''$  (0.005 pc) using the Combined Array for Research in Millimeter-wave Astronomy (CARMA). From Figure 2(c-e), for OMC-1, the orientation of the small scale  $B$ -field revealed by the CARMA largely follows that of the intermediate scale  $B$ -field seen by the JCMT POL-2, though a small fraction of the CARMA  $B$ -field half-vectors are offset from parallel to even perpendicular to the JCMT  $B$ -field half-vectors; for OMC-2, the small scale  $B$ -field is apparently decoupled from that on the intermediate scale and there is no obvious correlation between the orientations of the  $B$ -fields on the two scales; for OMC-3, the small scale and intermediate scale  $B$ -fields both appear to be uniform with the almost same orientation. There have been new ALMA observations of dust polarization toward several sources in the ISF; however, these observations were made at sub-arcsec resolutions, either probing  $B$ -field structures at too small scales to be compared with the JCMT data (Cortes et al. 2021) or being dominated by self-scattering and thus unable to probe the  $B$ -field structure (Takahashi et al. 2019; Liu et al. 2024).

More quantitatively, we compare the intermediate scale  $B$ -field probed by JCMT POL-2 with the large scale  $B$ -field probed by *Planck* by calculating the difference angle,  $\Delta\theta_B$ , between the orientations of the  $B$ -fields on the two scales. Since the *Planck* map covers an area much larger than that is covered by the JCMT map, we calculate  $\Delta\theta_B$  for each half-vector at  $8''$  interval in the JCMT map; the  $B$ -field orientation at the corresponding position in the *Planck* map is derived by a weighted average of the  $B$ -field orientations at the nearest four pixels, where the pixel size of the *Planck* map is  $2'$  and the weighting is taken as the inverse of the square of the distance between the pixel center to the position of interest. In Figure 2(f), the histogram of  $\Delta\theta_B$  for OMC-1 is clearly peaking toward  $0^\circ$ , suggesting that the orientation of the intermediate scale (0.03 pc)  $B$ -field is predominantly parallel with that of the large scale (0.6 pc)  $B$ -field. For OMC-2,  $\Delta\theta_B$  appears to be widely distributed between  $0^\circ$  and  $90^\circ$ , with a very minor tendency of peaking at  $0^\circ$ , indicating that the  $B$ -field orientation on the intermediate scale has shown strong local variation and started to decouple from that on the large scale. For OMC-3,  $\Delta\theta_B$  are almost all below  $35^\circ$ , indicating that the intermediate scale  $B$ -field is well aligned with that on the large scale.

Similarly to  $\Delta\theta_B$ , we compute the difference angle,  $\delta\theta_B$ , between the orientations of the  $B$ -fields probed by JCMT and CARMA, for each CARMA detection. Again the  $B$ -field orientation at the corresponding position in the JCMT map is derived by a weighted average of the  $B$ -field orientations at the nearest four pixels, and the weighting is taken as the inverse of the square of the distance between the pixel center to the position of interest. In Figure 2(g): the distribution of  $\delta\theta_B$  for OMC-1 shows a clear peak at  $0$ - $10^\circ$ , and gradually declines toward  $90^\circ$ ; for OMC-2,  $\delta\theta_B$  has a nearly flat distribution, again indicating that the  $B$ -fields on the two scales are apparently decoupled; for OMC-3, the distribution of  $\delta\theta_B$  depicts that the  $B$ -field orientation almost do not change across the two scales.

### 3.3. Relations between $B$ -field and filamentary structures

To investigate how the  $B$ -field orientation is aligned with the filamentary structures in the ISF, we employed the `filfinder` algorithm (Koch & Rosolowsky 2015) to extract filament skeletons. Figure 3(a) shows the derived skeletons along the main filament, the branches connected to the main filament, and some minor structures detached from the main filament. To quantify the filament orientations, we utilize the Principle Component Analysis (PCA) method on 10 adjacent pixels of the skeletons to determine the PA of the filaments at each position. We then compute the difference angles between the filament and  $B$ -field orientations. In Figure 3(a), the color scale of the skeletons visualizes the spatial distribution of the difference angles. Figures 3(b-d) show the histograms of the difference angles for OMC-1, OMC-2, and OMC-3, respectively. Along the filamentary cloud, three drastically different distributions for the relative orientation between the  $B$ -fields and filaments are seen: a bimodal distribution for OMC-1, nearly flat distribution for OMC-2, and a distribution with a predominant single peak at  $90^\circ$  for OMC-3. From the skeleton color scale representing the difference angles (Figure 3a), we can see that the bimodal distribution in OMC-1 is due to a combined effect that along the main filament, the  $B$ -field orientation is perpendicular to the filament axis, while along the relatively low density branches, the  $B$ -field orientation is parallel to the branch axis; on the other hand, for the distribution of relative orientation in OMC-3, a tail toward  $0^\circ$  is mostly attributed to OMC-3 South.

Molecular filaments may have complex internal structures, such as intertwined filamentary bundles or fibers. We identified the fibers with the `filfinder` algorithm from  $\text{N}_2\text{H}^+$  maps (see Appendix A). Figure 3(e) shows a comparison between the  $B$ -field orientations derived from our POL-2 observations and the fiber structures revealed by the combined ALMA and IRAM 30m  $\text{N}_2\text{H}^+$  (1-0) observations of OMC-1, 2 (Hacar et al. 2018). Such a comparison for OMC-3 is shown in Figure 3(f), where the ALMA  $\text{N}_2\text{H}^+$  (1-0) data were taken from Zhang et al. (2020). We calculate the



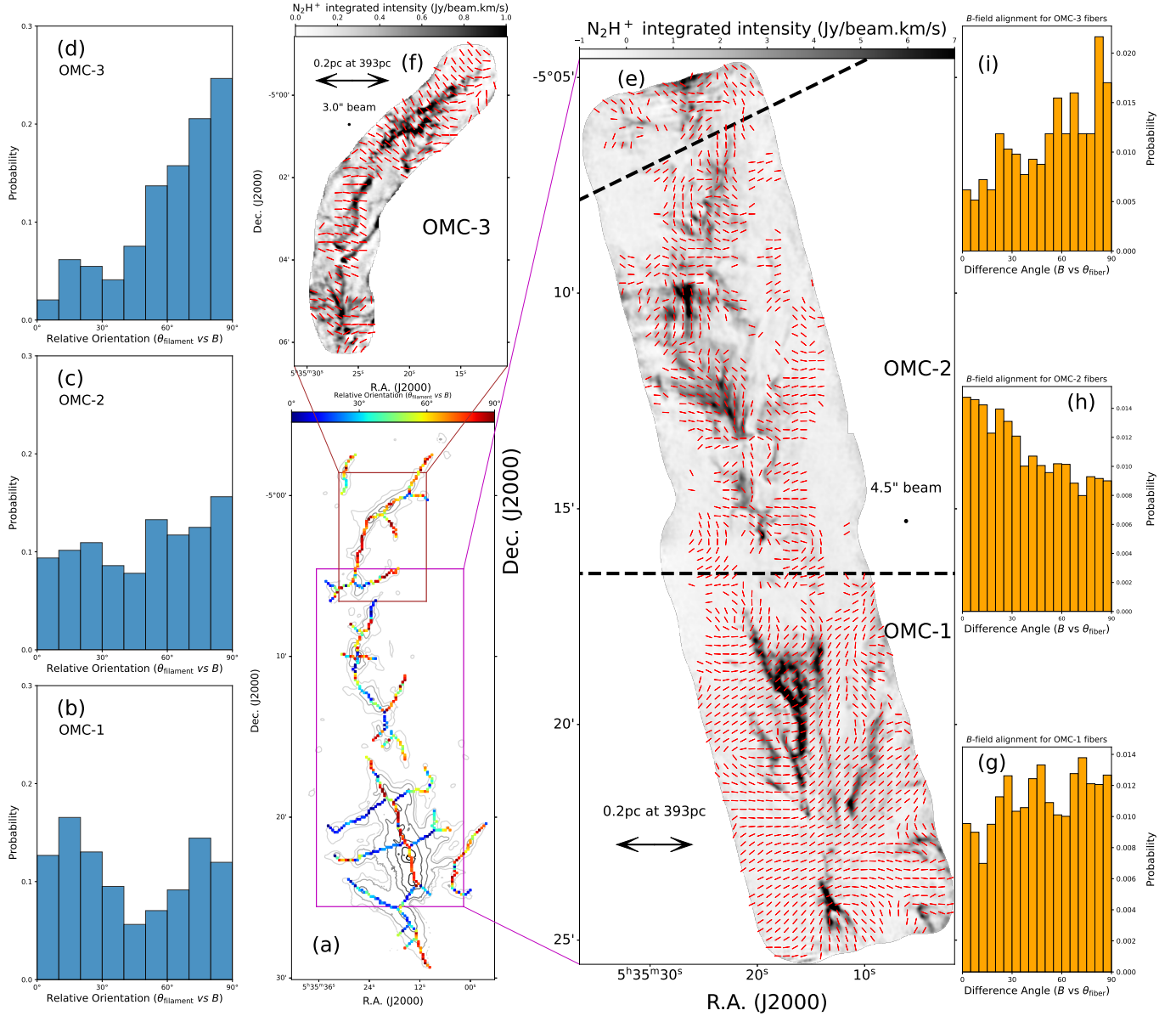


**Figure 3.** Panel (a): Colored points show locations along the skeleton of each filament where the filament orientation is compared with the  $B$ -field orientation, and the color scale denotes the derived difference angle between the two orientations, as indicated by a color bar on the top; the  $850\ \mu\text{m}$  total intensity is shown in contours with levels at a  $\log_{10}$  scale ( $\text{mJy beam}^{-1}$ ), starting from 2.2 and continuing at steps of 0.5. Panels (b), (c), and (d): Histograms of the difference angles between the filament skeleton and  $B$ -field orientations for OMC-1, OMC-2, and OMC-3. Panel (e): Red vectors plotted at an interval of  $12''$  show the  $B$ -field orientations derived by the JCMT POL-2, and the gray scale image shows the  $\text{N}_2\text{H}^+$  (1-0) velocity integrated emission in OMC-1 and OMC-2 (Hacar et al. 2018). Panel (f): the same as Panel (e), but for OMC-3, and the  $\text{N}_2\text{H}^+$  data are taken from (Zhang et al. 2020). Panels (g), (h), and (i) show the histograms of the difference angles between the  $\text{N}_2\text{H}^+$  fibers and POL-2  $B$ -field orientations in OMC-1, OMC-2, and OMC-3, respectively.

difference angles between the fiber and  $B$ -field orientations, as shown in Figure 3(g-i). In OMC-1, the fibers tend to be perpendicular to the  $B$ -field; this is not difficult to understand considering the bimodal distribution for the relative orientation between the  $B$ -field and filaments (Figure 3b) and here the fibers traced by the  $\text{N}_2\text{H}^+$  emission represent the high-density part of the filaments. In OMC-3, the fibers are clearly perpendicular to the  $B$ -field, consistent with the distribution of relative orientation between the  $B$ -field and filaments. Interestingly, the fibers in OMC-2 appear

to be predominantly parallel to the  $B$ -field, in contrast to the random distribution of relative orientation between the  $B$ -field and filaments.

#### 4. DISCUSSION AND SUMMARY

##### 4.1. *A tale of three: gravitational, turbulent, and magnetic interpretations for OMC-1, 2, and 3, respectively*

We have presented JCMT POL-2 dust polarization observations of a remarkable molecular filament containing OMC-1, OMC-2, and OMC-3 in the Orion ISF. Combing the POL-2 data with the *Planck* and CARMA polarization observations, we clearly see how the  $B$ -fields vary from the large ( $\sim 0.6$  pc) to intermediate ( $\sim 0.03$  pc) and small ( $\sim 0.005$ ) scales: for OMC-1, the  $B$ -field retains its mean orientation on all the scales, with some local variations on intermediate to small scales; for OMC-2, the  $B$ -fields on different scales are apparently decoupled, showing relatively disordered morphology on the intermediate and small scales; for OMC-3, the  $B$ -field shows a uniform morphology and the orientation does not change all the way from the large to intermediate and small scales. A natural and straightforward interpretation of such  $B$ -field morphologies, in particular their variation across different scales, is that the  $B$ -field in OMC-1 is channeling the gas accretion from the ambient medium to the filament, but as the mass continues to grow, forming massive dense cores within the filament, gravity overcomes the magnetic force, pulling the  $B$ -field into an hour-glass shape (see also [Ward-Thompson et al. 2017](#); [Pattle et al. 2017](#)). The  $B$ -field in OMC-2 appears highly twisted on the intermediate and small scales, suggesting that turbulence is dominating over the  $B$ -field; the  $B$ -field in OMC-3, especially OMC-3 North, has a nearly uniform morphology from large to small scales, indicating that the  $B$ -field is strong enough to dominate the gas dynamics (e.g., [Ostriker et al. 2001](#)). Below we test this simple interpretation by comparing the orientations between the  $B$ -fields and the dense gas structures.

Filamentary clouds naturally define an axis to be compared to the  $B$ -field, and such a comparison for ISF reveals again a trio: bimodal for OMC-1, random for OMC-2, and perpendicular for OMC-3 (Figures 3b-d). It immediately renders strong support to the above ternary interpretation. The bimodal distribution for the relative orientation between the  $B$ -field and filaments in OMC-1 is clearly correlated to the gas density, with the high-density filament skeleton perpendicular to the  $B$ -field and low-density skeletons parallel to the  $B$ -field, consistent with the scenario that the  $B$ -field is channeling gas flows toward the high-density filament (e.g., [Ward-Thompson et al. 2017](#); [Pillai et al. 2020](#); [Girichidis 2021](#)). Such a correlation is strengthened by looking into the filament internal structures, i.e., the  $\text{N}_2\text{H}^+$  fibers: as the high-density part of the filament, the fibers are preferentially perpendicular to the  $B$ -field (Figure 3g). In OMC-2, the random distribution is apparently a consequence of the disordered nature of the  $B$ -field structure. Very interestingly, the fibers in OMC-2 are largely parallel to the  $B$ -field (Figure 3h), showing a pattern that is consistent with the results of simulations of super-Alfvénic turbulence (see, e.g., Figure 2 and Figure 3 in [Padoan et al. 2001](#)), suggesting that turbulence is dynamically more important than the  $B$ -field in OMC-2. For OMC-3, the  $B$ -field is simply perpendicular to both the filament (Figure 3d) and fibers (Figure 3i), indicating that the  $B$ -field is strong enough to counteract gravity and turbulence.

##### 4.2. *The $B$ -field strength estimates*

To further quantify the impact of the  $B$ -field on the dynamical evolution of the filament, it is desirable to estimate the  $B$ -field strength. However, deriving the  $B$ -field strength with the David-Chandrasekhar-Fermi (DCF) method ([Davis 1951](#); [Chandrasekhar & Fermi 1953](#)) or its variants is subject to large uncertainty and in some cases is not applicable ([Liu et al. 2021, 2022a,b](#); [Chen et al. 2022](#)). First, the method requires calculation of the polarization angle dispersion due to turbulent disturbance, or decomposing the  $B$ -field into turbulent and ordered components and calculating their ratio. This step is not always feasible, especially when the  $B$ -field structure is complicated. Second, under the assumption of energy equipartition between turbulence and the turbulent  $B$ -field, and adopting a gas density and turbulent velocity dispersion obtained from other observations, the plane-of-sky (PoS)  $B$ -field strength can be derived. It should be noted that the energy equipartition assumption may not be valid when the  $B$ -field is weak. The estimates of the gas density and turbulent velocity dispersion often suffer large uncertainties. Nevertheless, the method has been widely used. Several such estimates for the sources in the ISF exist in the literature, and the results vary a lot, ranging from 0.3 to 6.6 mG for OMC-1 and from 0.13 to 0.64 mG for OMC-3 ([Matthews et al. 2005](#); [Vallée & Fiege 2007](#); [Hildebrand et al. 2009](#); [Houde et al. 2009](#); [Poidevin et al. 2013](#); [Pattle et al. 2017](#); [Chuss et al. 2019](#); [Guerra et al. 2021](#); [Hwang et al. 2021](#); [Li et al. 2022](#); [Zielinski & Wolf 2022](#)). Here we try with the best effort to estimate the PoS  $B$ -field strengths in the three regions with the new data, obtaining 0.45, 0.25, and 0.37 mG for OMC-1, 2, and 3, respectively (see Appendix B).

Given the aforementioned cautions and uncertainties, we only make a comparative rather than more detailed quantitative analysis based on the derived  $B$ -field strengths. It is worth mentioning that OMC-1 has a width about two times greater than OMC-2 and 3 under a same column density threshold, resulting in a volume density in this region slightly lower than that in the latter two. But about half of the gas mass in OMC-1 is attributed to the central high-density part with a width of  $\sim 0.06$  pc, and within that area the average volume density reaches  $2.5 \times 10^6 \text{ cm}^{-3}$ . Therefore, though the  $B$ -field in OMC-1 is stronger, considering a much greater mass and central density, it is completely plausible that gravity is overwhelmingly more important in this region. OMC-2 and 3 have almost the same mass and non-thermal velocity dispersion (see Appendix B), while the  $B$ -field in OMC-3 is stronger than that in OMC-2; the relative  $B$ -field strength of the two regions is at least compatible with the interpretation that turbulence in OMC-2 and  $B$ -field in OMC-3 is taking a leading role.

#### 4.3. *The impact of magnetic field on star formation*

Given the markedly different  $B$ -field properties across the three regions in the ISF, it is of great interest to examine how the star formation activity is affected. We collect a catalog of Young Stellar Objects (YSOs), which are classified into Class 0, Class I, flat-spectrum, and disk-bearing pre-main-sequence stars, based on the works of (Megeath et al. 2012; Furlan et al. 2016; Großschedl et al. 2019). Figure 4 shows all the YSOs in the OMC-1, 2, and 3, and the statistics of each type in each of the three regions. The star formation activity in OMC-1 is far more vigorous and complicated than that in OMC-2 and 3. OMC-1 is the only region of the three forming high-mass stars, containing several well-known high-mass protostellar objects. It is located behind the luminous Trapezium cluster, which is the central part of the Orion Nebular Cluster (ONC). The collected YSOs in this region is completely dominated by the disk sources, and are heavily contaminated by the foreground ONC sources (Lada et al. 2000; Otter et al. 2021). Here we focus on the comparison between OMC-2 and OMC-3. From Figure 4, OMC-2 has a higher fraction of disk sources (50/78) than OMC-3 (20/43), indicating a younger age of the cluster in OMC-3. The total number of YSOs in OMC-2 is higher than that in OMC-3. Note that the mass, mean density, and non-thermal velocity dispersion in the two regions are almost the same, and the only appreciable difference lies in the  $B$ -field geometries and the relative orientation between the  $B$ -fields and filaments/fibers. Therefore the differing YSO populations in the two regions are mostly likely due to the  $B$ -field effect, providing compelling evidence that a dynamically more important  $B$ -field leads to slower (or delayed) and less efficient star formation in molecular clouds.

To summarize, concerning which mechanism is shaping the dynamics of molecular clouds on  $\sim 0.01$  to 1 pc scales, each of the three clouds (OMC-1, 2, and 3 in the Orion ISF) seems to be telling a different story based on our JCMT POL-2 observations along with the *Planck* and CARMA data. Therefore it is probably an over-simplified interpretation to claim that either magnetic field or turbulence is universally more important in molecular cloud evolution and star formation. By comparing the YSO populations in OMC-2 and 3, we find evidence that a strong  $B$ -field could make star formation relatively slower and less efficient. Zhang et al. (2019) carried out MHD simulations of sub-Alfvénic molecular clouds, focusing on the  $B$ -field orientation variation across various scales. They found that on small ( $< 0.1$  pc) scales, the cores are super-Alfvénic, as a consequence of turbulent energy concentration induced by gravity, and thus the  $B$ -field on small scales exhibits a wide range of deviation in orientation from that on large scales. If one takes an average  $B$ -field orientation for each of the dense cores in the CARMA maps (Figure 2c-e) and compare to the  $B$ -field revealed by *Planck*, the offset distribution could be to some extent consistent with the work of Zhang et al. (2019). However, a detailed comparison shows that the cross-scale correlation in  $B$ -field orientation (Figure 2f, g) is distinctly different from region to region, certainly not random in OMC-1 and 3. The observed relation between the  $B$ -field and filament/fiber orientations and the star formation activity variation further suggest a tale-of-three interpretation of the three regions regarding the interplay between gravity,  $B$ -field, and turbulence.

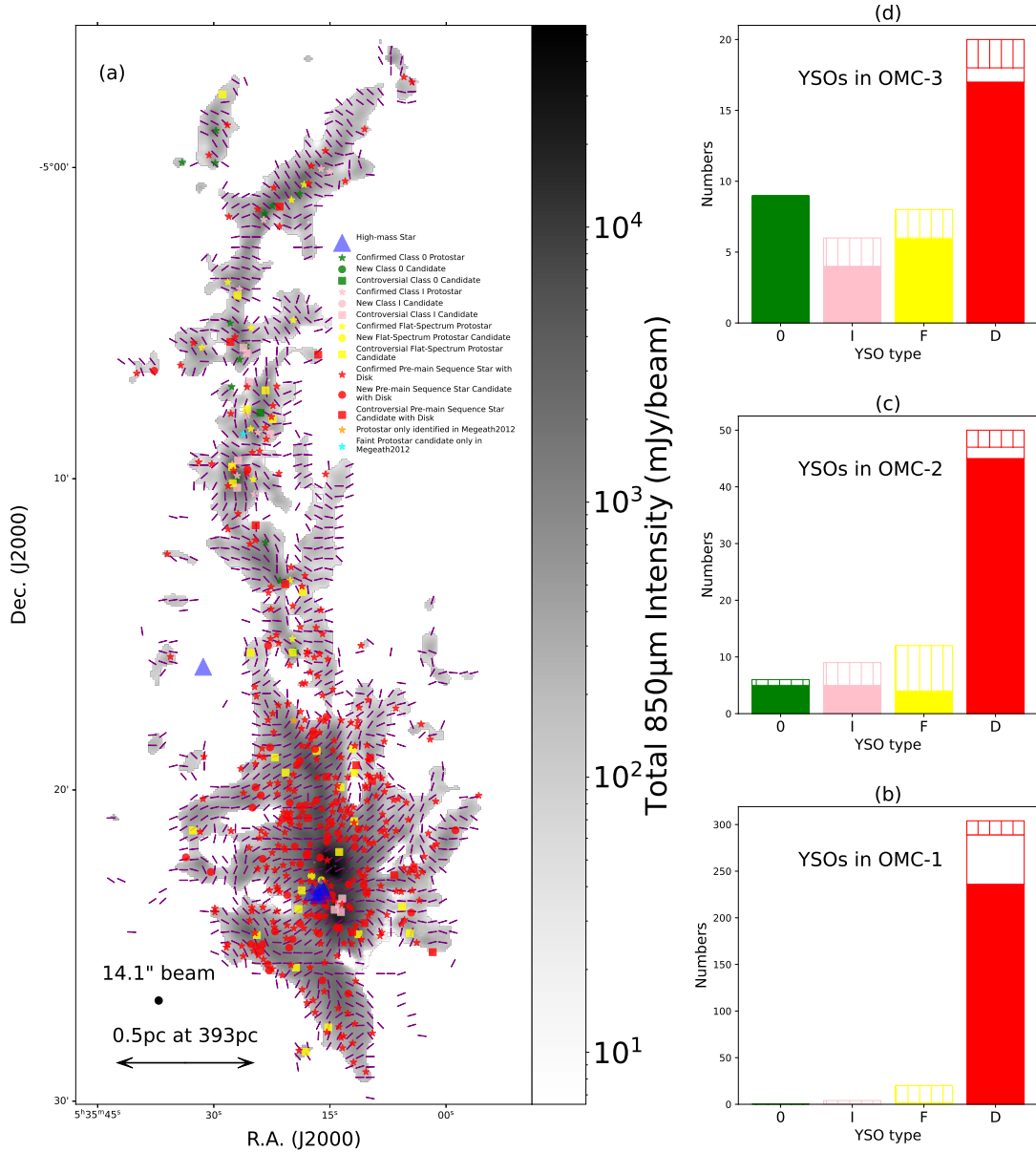


**Figure 4.** Panel (a): Distribution of detected YSOs overlaid on the  $B$ -field orientation maps. All the YSO candidates and high-mass stars are taken from the literature (Megeath et al. 2012; Furlan et al. 2016; Großschedl et al. 2019). Purple vectors at a  $20''$  interval indicate the  $B$ -field orientations observed by the JCMT POL-2. The Class 0, Class I, flat-spectrum sources, and pre-main sequence stars with disks are denoted in green, pink, yellow, and red colors, respectively. For each YSO type, the confirmed ones that are consistent in different literature are represented by star symbols; newly discovered candidates by Großschedl et al. (2019) are indicated with filled circles; controversial candidates, showing inconsistencies in different literature, are marked with filled squares. Panels (b), (c), and (d): Histograms of the four YSO types in OMC-1, OMC-2, and OMC-3, respectively; Class 0, Class I, flat-spectrum sources, and pre-main sequence stars with disks are labeled as ‘0’, ‘I’, ‘F’, and ‘D’, respectively, with the same colors as in Panel (a); filled histograms represent confirmed YSOs, hollow histograms depict newly discovered YSOs, and vertical gridded histograms indicate controversial YSOs.

This work is supported by the National Natural Science Foundation of China (NSFC) grants No. 12425304 and No. U1731237, the National Key R&D Program of China with No. 2023YFA1608204 and No. 2022YFA1603103, and the science research grant from the China Manned Space Project with no. CMS-CSST-2021-B06. J.W. thanks Chao Zhang, Nan-Nan Yue, Di Li, Qizhou Zhang for generously providing us the  $\text{N}_2\text{H}^+$  data that covered OMC-2 and OMC-3 in Orion for the analysis of fiber structures. C.E. acknowledges the financial support from the grant R.JF/2020/000071 as a part of the Ramanujan Fellowship awarded by the Science and Engineering Research Board (SERB). The James Clerk Maxwell Telescope is operated by the East Asian Observatory on behalf of The National Astronomical Observatory of Japan; Academia Sinica Institute of Astronomy and Astrophysics; the Korea Astronomy and Space Science Institute; Center for Astronomical Mega-Science (as well as the National Key R&D Program of China with No. 2017YFA0402700). Additional funding support is provided by the Science and Technology Facilities Council of the United Kingdom and participating universities in the United Kingdom, Canada, and Ireland. Additional funds for the construction of SCUBA-2 and POL-2 were provided by the Canada Foundation for Innovation.

## APPENDIX

### A. IDENTIFIED FIBER STRUCTURES

The fibers within the filament are extracted using the filfinder algorithm from the  $\text{N}_2\text{H}^+$  (1-0) velocity integrated emission maps. Figure 5 shows a comparison between the derived fibers, the  $\text{N}_2\text{H}^+$  emission, and the total 850  $\mu\text{m}$  emission.

### B. DETAILS FOR B-FIELD STRENGTH CALCULATION

In the DCF assumption, the PoS  $B$ -field strength of the molecular cloud is estimated by interpreting the observed deviation of polarization angles from a mean polarization angle distribution as a result of Alfvén waves induced by turbulent perturbations. i.e.:

$$B_0 = \sigma_v \sqrt{\mu_0 \rho} \left( \frac{\delta B}{B_0} \right)^{-1} \quad (\text{B1})$$

where  $\sigma_v$  represents the turbulence-induced velocity dispersion which could approximately equate to the non-thermal velocity dispersion,  $\rho$  denotes the gas mass density.  $\delta B/B_0$  denotes the turbulent-to-ordered magnetic field ratio.

To obtain the mass density, we modeled the three star-forming clouds within the Orion A ISF as cylindrical filaments. We use the column density map at  $\sim 8''$  resolution produced by Schuller et al. (2021) to measure the mass of the three regions, obtaining  $\sim 660$ ,  $\sim 250$ , and  $\sim 260 M_\odot$  for OMC-1, 2, 3. The dimensions of the three regions are measured to be approximately  $0.93 \text{ pc} \times 0.23 \text{ pc}$  for OMC-1,  $1.0 \text{ pc} \times 0.1 \text{ pc}$  for OMC-2, and  $1.0 \text{ pc} \times 0.1 \text{ pc}$  for OMC-3. Assuming a cylinder geometry lying in the plane of sky, the volume densities are found to be  $\sim 2.4 \times 10^5$ ,  $\sim 4.5 \times 10^5$ , and  $\sim 4.7 \times 10^5 \text{ cm}^{-3}$  for OMC-1, 2, and 3, respectively.

To estimate the velocity dispersion in the ISF, we utilized the  $\text{NH}_3$  (1,1) observation data from the Green Bank Ammonia Survey (GAS, Friesen et al. 2017) with a resolution of  $36''$ . To extract the non-thermal velocity dispersion, we subtracted the thermal components of the observed velocity dispersion with the temperature map provided by Schuller et al. (2021). Our analysis revealed that the mean non-thermal velocity dispersion in OMC-1, OMC-2, and OMC-3 is  $0.90 \text{ km s}^{-1}$ ,  $0.38 \text{ km s}^{-1}$ , and  $0.41 \text{ km s}^{-1}$ , respectively.

The turbulent-to-ordered magnetic field ratio  $\delta B/B_0$  is determined by the dispersion of polarization angles. However, quantifying the turbulent  $B$ -field components could have bias due to the effects of non-turbulent field structure in dense clouds. So the angular dispersion function method has been developed to reduce the bias. Moreover, by considering the effect of signal integration along the line of sight and within the beam in the analysis, Houde et al. (2009) proposed the Autocorrelation Function (ACF) form to precisely derive the turbulent-to-ordered magnetic field ratios. The angular dispersion function could be expressed as:

$$1 - \langle \cos[\Delta\Phi(l)] \rangle \simeq \frac{1}{N} \frac{\langle \delta B^2 \rangle}{\langle B_0^2 \rangle} \times [1 - e^{-l^2/2(\delta^2+2W^2)}] + a_2 l^2 \quad (\text{B2})$$

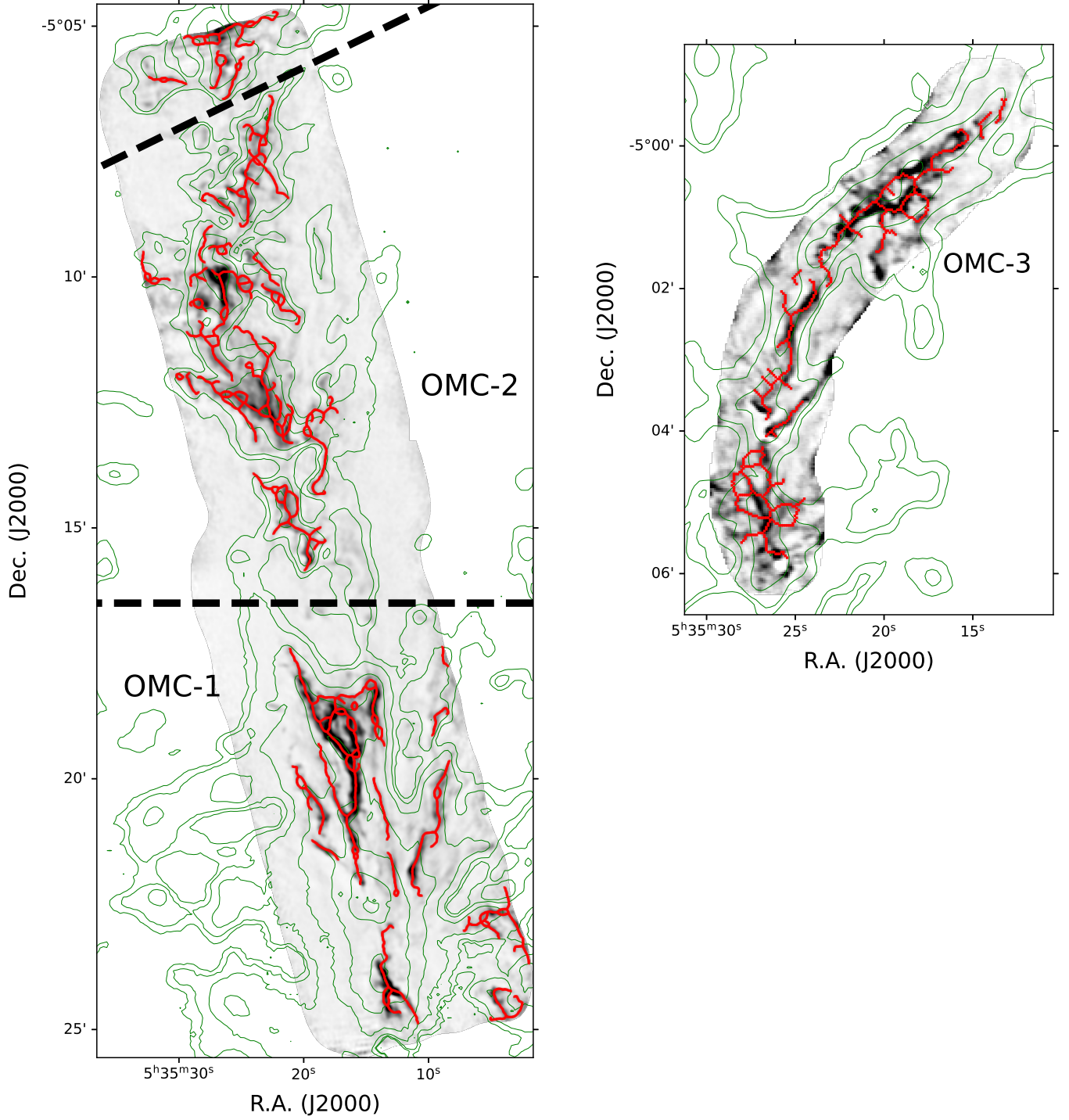


**Figure 5.** Gray scale images show the velocity integrated  $\text{N}_2\text{H}^+$  (1-0) emissions, overlaid with the extracted fibers shown in red lines and the total  $850\ \mu\text{m}$  intensity shown in green contours. The left panel shows the OMC-1, 2 region, with the  $\text{N}_2\text{H}^+$  data taken from (Hacar et al. 2018), and the right panel shows OMC-3, with the  $\text{N}_2\text{H}^+$  data taken from (Zhang et al. 2020).

where  $N$  is the number of turbulent cells probed by the telescope beam.  $\Delta\Phi(l)$  represents the position angle differences of two vectors at a distance  $l$ ,  $a_2$  signifies the slope of the second-order term in the Taylor expansion.

$$N = \frac{(\delta^2 + 2W^2)\Delta'}{\sqrt{2\pi}\delta^3}, \quad (\text{B3})$$

$W$  denotes the beam radius (6.0'' for JCMT 850 $\mu$ m observations),  $\Delta'$  depicts the cloud depth and  $\delta$  stands for the turbulent correlation length.

Setting cloud depths to 0.23pc, 0.1pc and 0.1pc for OMC-1, OMC-2, and OMC-3 respectively, we derived the ACF of the three clouds with the JCMT POL-2 polarization vectors (2952 vectors in OMC-1, 1118 vectors in OMC-2, 890 vectors in OMC-3). Equation B2 is valid when  $l$  is not too big compared to a few times of  $W$  (Houde et al. 2009). In addition, we have a polarization map with a finite size, and thus the number of polarization detections on which the ACF could be derived at high intensities decreases as  $l$  increases, leading to degrading statistics for the data points on large  $l$ . We therefore limit our fitting to the data points with  $l < 100''$ . In Figure 6, the fitting results revealed that OMC-3 has the smallest  $\delta B/B_0$  value of 0.596 and OMC-2 has the largest  $\delta B/B_0$  value of 0.807. While OMC-1 has a  $\delta B/B_0$  value of 0.770. We also obtain  $\delta=4.39$ , 3.15, and 4.08 mpc for OMC-1, 2, and 3, respectively, with the fitting. We note that  $\delta$  cannot be resolved with a telescope beam of 27 mpc (14'' at a distance of 393 pc). Such an issue occurs in other works of applying the ACF fitting to dust polarization data (e.g., Houde et al. 2009; Qiu et al. 2013). Thus the inferred  $\delta$  is more like a numerical artifact from the fitting, and the turbulence correlation scale is still to be explored. We finally estimated the strength of the PoS component of the  $B$ -field for OMC-1, OMC-2, and OMC-3 as 0.45 mG, 0.25 mG, and 0.37 mG, respectively.

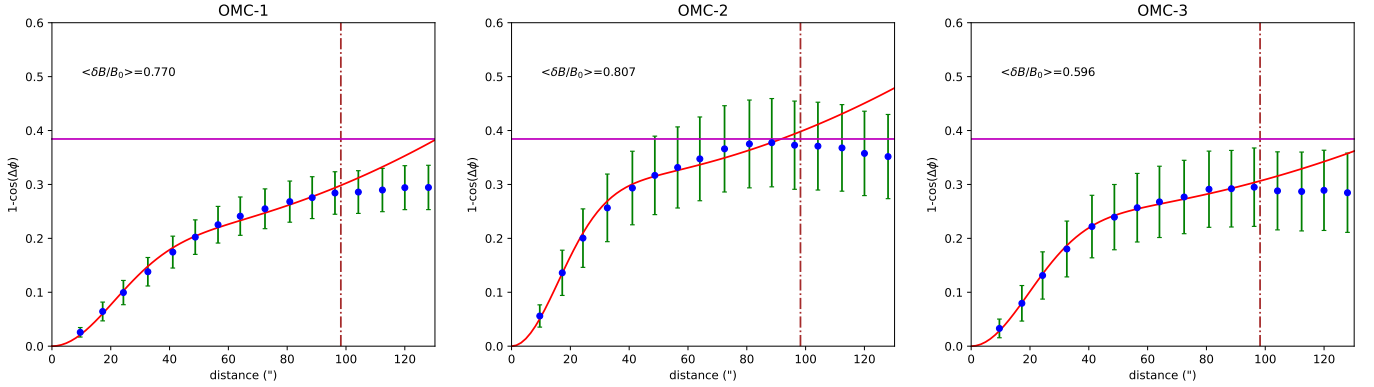


**Figure 6.** Fitting results of the ACF for OMC-1, 2, and 3 from left to right. For each panel, blue filled circles with error bars denote data points derived from the polarization observations; the best fitting result is shown by a red solid line; a horizontal magenta line marks the value expected for a random field (52°, Poidevin et al. 2010); a vertical brown dashed line marks the right boundary of the points to be fitted.

## REFERENCES

- Ajeddig, H., Adam, R., Ade, P., et al. 2022, in European Physical Journal Web of Conferences, Vol. 257, mm Universe @ NIKA2 - Observing the mm Universe with the NIKA2 Camera, 00002, doi: [10.1051/epjconf/202225700002](https://doi.org/10.1051/epjconf/202225700002)
- André, P., Di Francesco, J., Ward-Thompson, D., et al. 2014, in Protostars and Planets VI, ed. H. Beuther, R. S. Klessen, C. P. Dullemond, & T. Henning, 27, doi: [10.2458/azu\\_uapress.9780816531240-ch002](https://doi.org/10.2458/azu_uapress.9780816531240-ch002)
- Arzoumanian, D., Furuya, R. S., Hasegawa, T., et al. 2021, A&A, 647, A78, doi: [10.1051/0004-6361/202038624](https://doi.org/10.1051/0004-6361/202038624)
- Bailer-Jones, C. A. L., Rybizki, J., Foesneau, M., Demleitner, M., & Andrae, R. 2021, AJ, 161, 147, doi: [10.3847/1538-3881/abd806](https://doi.org/10.3847/1538-3881/abd806)
- Bally, J. 2008, Overview of the Orion Complex, ed. B. Reipurth, Vol. 4, 459
- Bastien, P. 2020, in Stellar Magnetism: A Workshop in Honour of the Career and Contributions of John D. Landstreet, ed. G. Wade, E. Alecian, D. Bohlender, & A. Sigut, Vol. 11, 117–124
- Chandrasekhar, S., & Fermi, E. 1953, ApJ, 118, 113, doi: [10.1086/145731](https://doi.org/10.1086/145731)
- Chen, C.-Y., Li, Z.-Y., Mazzei, R. R., et al. 2022, MNRAS, 514, 1575, doi: [10.1093/mnras/stac1417](https://doi.org/10.1093/mnras/stac1417)
- Chini, R., Reipurth, B., Ward-Thompson, D., et al. 1997, ApJL, 474, L135, doi: [10.1086/310436](https://doi.org/10.1086/310436)
- Chuss, D. T., Andersson, B. G., Bally, J., et al. 2019, ApJ, 872, 187, doi: [10.3847/1538-4357/aafd37](https://doi.org/10.3847/1538-4357/aafd37)

- Cortes, P. C., Le Gouellec, V. J. M., Hull, C. L. H., et al. 2021, *ApJ*, 907, 94, doi: [10.3847/1538-4357/abcafb](https://doi.org/10.3847/1538-4357/abcafb)
- Cox, N. L. J., Arzoumanian, D., André, P., et al. 2016, *A&A*, 590, A110, doi: [10.1051/0004-6361/201527068](https://doi.org/10.1051/0004-6361/201527068)
- Crutcher, R. M. 2012, *ARA&A*, 50, 29, doi: [10.1146/annurev-astro-081811-125514](https://doi.org/10.1146/annurev-astro-081811-125514)
- Currie, M. J., & Berry, D. S. 2014, KAPPA: Kernel Applications Package. <http://ascl.net/1403.022>
- Currie, M. J., Berry, D. S., Jenness, T., et al. 2014, in *Astronomical Society of the Pacific Conference Series*, Vol. 485, *Astronomical Data Analysis Software and Systems XXIII*, ed. N. Manset & P. Forshay, 391
- Davis, L. 1951, *Physical Review*, 81, 890, doi: [10.1103/PhysRev.81.890.2](https://doi.org/10.1103/PhysRev.81.890.2)
- Dempsey, J. T., Friberg, P., Jenness, T., et al. 2013, *MNRAS*, 430, 2534, doi: [10.1093/mnras/stt090](https://doi.org/10.1093/mnras/stt090)
- Friberg, P., Bastien, P., Berry, D., et al. 2016, in *Society of Photo-Optical Instrumentation Engineers (SPIE) Conference Series*, Vol. 9914, *Millimeter, Submillimeter, and Far-Infrared Detectors and Instrumentation for Astronomy VIII*, ed. W. S. Holland & J. Zmuidzinas, 991403, doi: [10.1117/12.2231943](https://doi.org/10.1117/12.2231943)
- Friesen, R. K., Pineda, J. E., co-PIs, et al. 2017, *ApJ*, 843, 63, doi: [10.3847/1538-4357/aa6d58](https://doi.org/10.3847/1538-4357/aa6d58)
- Furlan, E., Fischer, W. J., Ali, B., et al. 2016, *ApJS*, 224, 5, doi: [10.3847/0067-0049/224/1/5](https://doi.org/10.3847/0067-0049/224/1/5)
- Gaia Collaboration, Brown, A. G. A., Vallenari, A., et al. 2021, *A&A*, 649, A1, doi: [10.1051/0004-6361/202039657](https://doi.org/10.1051/0004-6361/202039657)
- Girichidis, P. 2021, *MNRAS*, 507, 5641, doi: [10.1093/mnras/stab2157](https://doi.org/10.1093/mnras/stab2157)
- Großschedl, J. E., Alves, J., Meingast, S., et al. 2018, *A&A*, 619, A106, doi: [10.1051/0004-6361/201833901](https://doi.org/10.1051/0004-6361/201833901)
- Großschedl, J. E., Alves, J., Teixeira, P. S., et al. 2019, *A&A*, 622, A149, doi: [10.1051/0004-6361/201832577](https://doi.org/10.1051/0004-6361/201832577)
- Guerra, J. A., Chuss, D. T., Dowell, C. D., et al. 2021, *ApJ*, 908, 98, doi: [10.3847/1538-4357/abd6f0](https://doi.org/10.3847/1538-4357/abd6f0)
- Hacar, A., Clark, S. E., Heitsch, F., et al. 2023, in *Astronomical Society of the Pacific Conference Series*, Vol. 534, *Protostars and Planets VII*, ed. S. Inutsuka, Y. Aikawa, T. Muto, K. Tomida, & M. Tamura, 153, doi: [10.48550/arXiv.2203.09562](https://doi.org/10.48550/arXiv.2203.09562)
- Hacar, A., Tafalla, M., Forbrich, J., et al. 2018, *A&A*, 610, A77, doi: [10.1051/0004-6361/201731894](https://doi.org/10.1051/0004-6361/201731894)
- Henebelle, P., & Inutsuka, S.-i. 2019, *Frontiers in Astronomy and Space Sciences*, 6, 5, doi: [10.3389/fspas.2019.00005](https://doi.org/10.3389/fspas.2019.00005)
- Hildebrand, R. H., Kirby, L., Dotson, J. L., Houde, M., & Vaillancourt, J. E. 2009, *ApJ*, 696, 567, doi: [10.1088/0004-637X/696/1/567](https://doi.org/10.1088/0004-637X/696/1/567)
- Holland, W. S., Bintley, D., Chapin, E. L., et al. 2013, *MNRAS*, 430, 2513, doi: [10.1093/mnras/sts612](https://doi.org/10.1093/mnras/sts612)
- Houde, M., Dowell, C. D., Hildebrand, R. H., et al. 2004, *ApJ*, 604, 717, doi: [10.1086/382067](https://doi.org/10.1086/382067)
- Houde, M., Vaillancourt, J. E., Hildebrand, R. H., Chitsazzadeh, S., & Kirby, L. 2009, *ApJ*, 706, 1504, doi: [10.1088/0004-637X/706/2/1504](https://doi.org/10.1088/0004-637X/706/2/1504)
- Hull, C. L. H., Plambeck, R. L., Kwon, W., et al. 2014, *ApJS*, 213, 13, doi: [10.1088/0067-0049/213/1/13](https://doi.org/10.1088/0067-0049/213/1/13)
- Hwang, J., Kim, J., Pattle, K., et al. 2021, *ApJ*, 913, 85, doi: [10.3847/1538-4357/abf3c4](https://doi.org/10.3847/1538-4357/abf3c4)
- Jenness, T., Chapin, E. L., Berry, D. S., et al. 2013, SMURF: Submillimeter User Reduction Facility. <http://ascl.net/1310.007>
- Johnstone, D., & Bally, J. 1999, *ApJL*, 510, L49, doi: [10.1086/311792](https://doi.org/10.1086/311792)
- Koch, E. W., & Rosolowsky, E. W. 2015, *MNRAS*, 452, 3435, doi: [10.1093/mnras/stv1521](https://doi.org/10.1093/mnras/stv1521)
- Lada, C. J., Muench, A. A., Haisch, Karl E., J., et al. 2000, *AJ*, 120, 3162, doi: [10.1086/316848](https://doi.org/10.1086/316848)
- Lazarian, A. 2007, *JQSRT*, 106, 225, doi: [10.1016/j.jqsrt.2007.01.038](https://doi.org/10.1016/j.jqsrt.2007.01.038)
- Li, D., Tang, X., Henkel, C., et al. 2020, *ApJ*, 901, 62, doi: [10.3847/1538-4357/abae60](https://doi.org/10.3847/1538-4357/abae60)
- Li, H.-B. 2021, *Galaxies*, 9, 41, doi: [10.3390/galaxies9020041](https://doi.org/10.3390/galaxies9020041)
- Li, P. S., Lopez-Rodriguez, E., Soam, A., & Klein, R. I. 2022, *MNRAS*, 514, 3024, doi: [10.1093/mnras/stac1527](https://doi.org/10.1093/mnras/stac1527)
- Liu, J., Qiu, K., & Zhang, Q. 2022a, *ApJ*, 925, 30, doi: [10.3847/1538-4357/ac3911](https://doi.org/10.3847/1538-4357/ac3911)
- Liu, J., Zhang, Q., Commerçon, B., et al. 2021, *ApJ*, 919, 79, doi: [10.3847/1538-4357/ac0cec](https://doi.org/10.3847/1538-4357/ac0cec)
- Liu, J., Zhang, Q., & Qiu, K. 2022b, *Frontiers in Astronomy and Space Sciences*, 9, 943556, doi: [10.3389/fspas.2022.943556](https://doi.org/10.3389/fspas.2022.943556)
- Liu, Y., Takahashi, S., Machida, M., et al. 2024, *ApJ*, 963, 104, doi: [10.3847/1538-4357/ad182d](https://doi.org/10.3847/1538-4357/ad182d)
- Lombardi, M., Bouy, H., Alves, J., & Lada, C. J. 2014, *A&A*, 566, A45, doi: [10.1051/0004-6361/201323293](https://doi.org/10.1051/0004-6361/201323293)
- Mac Low, M.-M., & Klessen, R. S. 2004, *Reviews of Modern Physics*, 76, 125, doi: [10.1103/RevModPhys.76.125](https://doi.org/10.1103/RevModPhys.76.125)
- Mairs, S., Dempsey, J. T., Bell, G. S., et al. 2021, *AJ*, 162, 191, doi: [10.3847/1538-3881/ac18bf](https://doi.org/10.3847/1538-3881/ac18bf)
- Matthews, B. C., Lai, S.-P., Crutcher, R. M., & Wilson, C. D. 2005, *ApJ*, 626, 959, doi: [10.1086/430127](https://doi.org/10.1086/430127)
- Matthews, B. C., McPhee, C. A., Fissel, L. M., & Curran, R. L. 2009, *ApJS*, 182, 143, doi: [10.1088/0067-0049/182/1/143](https://doi.org/10.1088/0067-0049/182/1/143)
- Matthews, B. C., Wilson, C. D., & Fiege, J. D. 2001, *ApJ*, 562, 400, doi: [10.1086/323375](https://doi.org/10.1086/323375)



- McKee, C. F., & Ostriker, E. C. 2007, *ARA&A*, 45, 565, doi: [10.1146/annurev.astro.45.051806.110602](https://doi.org/10.1146/annurev.astro.45.051806.110602)
- Megeath, S. T., Gutermuth, R., Muzerolle, J., et al. 2012, *AJ*, 144, 192, doi: [10.1088/0004-6256/144/6/192](https://doi.org/10.1088/0004-6256/144/6/192)
- Mouschovias, T. C., Tassis, K., & Kunz, M. W. 2006, *ApJ*, 646, 1043, doi: [10.1086/500125](https://doi.org/10.1086/500125)
- Ostriker, E. C., Stone, J. M., & Gammie, C. F. 2001, *ApJ*, 546, 980, doi: [10.1086/318290](https://doi.org/10.1086/318290)
- Otter, J., Ginsburg, A., Ballering, N. P., et al. 2021, *ApJ*, 923, 221, doi: [10.3847/1538-4357/ac29c2](https://doi.org/10.3847/1538-4357/ac29c2)
- Padoan, P., Goodman, A., Draine, B. T., et al. 2001, *ApJ*, 559, 1005, doi: [10.1086/322504](https://doi.org/10.1086/322504)
- Pattle, K., Ward-Thompson, D., Berry, D., et al. 2017, *ApJ*, 846, 122, doi: [10.3847/1538-4357/aa80e5](https://doi.org/10.3847/1538-4357/aa80e5)
- Pillai, T. G. S., Clemens, D. P., Reissl, S., et al. 2020, *Nature Astronomy*, 4, 1195, doi: [10.1038/s41550-020-1172-6](https://doi.org/10.1038/s41550-020-1172-6)
- Pineda, J. E., Arzoumanian, D., Andre, P., et al. 2023, in *Astronomical Society of the Pacific Conference Series*, Vol. 534, *Protostars and Planets VII*, ed. S. Inutsuka, Y. Aikawa, T. Muto, K. Tomida, & M. Tamura, 233, doi: [10.48550/arXiv.2205.03935](https://doi.org/10.48550/arXiv.2205.03935)
- Planck Collaboration, Ade, P. A. R., Aghanim, N., et al. 2015, *A&A*, 576, A104, doi: [10.1051/0004-6361/201424082](https://doi.org/10.1051/0004-6361/201424082)
- Plaszczynski, S., Montier, L., Levrier, F., & Tristram, M. 2014, *MNRAS*, 439, 4048, doi: [10.1093/mnras/stu270](https://doi.org/10.1093/mnras/stu270)
- Poidevin, F., Bastien, P., & Jones, T. J. 2011, *ApJ*, 741, 112, doi: [10.1088/0004-637X/741/2/112](https://doi.org/10.1088/0004-637X/741/2/112)
- Poidevin, F., Bastien, P., & Matthews, B. C. 2010, *ApJ*, 716, 893, doi: [10.1088/0004-637X/716/2/893](https://doi.org/10.1088/0004-637X/716/2/893)
- Poidevin, F., Falceta-Gonçalves, D., Kowal, G., de Gouveia Dal Pino, E., & Mário Magalhães, A. 2013, *ApJ*, 777, 112, doi: [10.1088/0004-637X/777/2/112](https://doi.org/10.1088/0004-637X/777/2/112)
- Qiu, K., Zhang, Q., Menten, K. M., Liu, H. B., & Tang, Y.-W. 2013, *ApJ*, 779, 182, doi: [10.1088/0004-637X/779/2/182](https://doi.org/10.1088/0004-637X/779/2/182)
- Rezaei Kh., S., Bailer-Jones, C. A. L., Soler, J. D., & Zari, E. 2020, *A&A*, 643, A151, doi: [10.1051/0004-6361/202038708](https://doi.org/10.1051/0004-6361/202038708)
- Schleuning, D. A. 1998, *ApJ*, 493, 811, doi: [10.1086/305139](https://doi.org/10.1086/305139)
- Schuller, F., André, P., Shimajiri, Y., et al. 2021, *A&A*, 651, A36, doi: [10.1051/0004-6361/202038259](https://doi.org/10.1051/0004-6361/202038259)
- Takahashi, S., Machida, M. N., Tomisaka, K., et al. 2019, *ApJ*, 872, 70, doi: [10.3847/1538-4357/aaf6ed](https://doi.org/10.3847/1538-4357/aaf6ed)
- Tang, Y.-W., Koch, P. M., Peretto, N., et al. 2019, *ApJ*, 878, 10, doi: [10.3847/1538-4357/ab1484](https://doi.org/10.3847/1538-4357/ab1484)
- Vallée, J. P., & Fiege, J. D. 2007, *AJ*, 133, 1012, doi: [10.1086/511004](https://doi.org/10.1086/511004)
- Ward-Thompson, D., Pattle, K., Bastien, P., et al. 2017, *ApJ*, 842, 66, doi: [10.3847/1538-4357/aa70a0](https://doi.org/10.3847/1538-4357/aa70a0)
- Zhang, C., Ren, Z., Wu, J., et al. 2020, *MNRAS*, 497, 793, doi: [10.1093/mnras/staa1958](https://doi.org/10.1093/mnras/staa1958)
- Zhang, Y., Guo, Z., Wang, H. H., & Li, H. b. 2019, *ApJ*, 871, 98, doi: [10.3847/1538-4357/aaf57c](https://doi.org/10.3847/1538-4357/aaf57c)
- Zielinski, N., & Wolf, S. 2022, *A&A*, 659, A22, doi: [10.1051/0004-6361/202141537](https://doi.org/10.1051/0004-6361/202141537)